International Journal of
Molecular Sciences

MDPI

Article

Physical Responses to the Structural Evolution of CL-20-Based Energetic Solvates with H_2O_2 and H_2O Under External Electric Field

Lu Shi [1,*], Li Fan [1], Huaya Sun [1] and Daichuan Ma [2]

[1] College of Chemistry and Materials Engineering, Mianyang Teachers' College, Mianyang 621000, China; 18280769523@163.com (L.F.); shy1738082@outlook.com (H.S.)
[2] Analytical & Testing Center, Sichuan University, Chengdu 610064, China; dcma@scu.edu.cn
* Correspondence: shilu@mtc.edu.cn

Abstract

The effects of an external electric field (EEF) on the crystal structure, nonbonded interaction, sensitivity, and mechanical properties of CL-20/H_2O_2 and CL-20/H_2O energetic solvates have been investigated by classical molecular dynamics simulations. Compared with CL-20/H_2O solvate, CL-20/H_2O_2 solvate possesses stronger O-H···O and C-H···O hydrogen-bond networks, which are more sensitive to the variation of electric field intensity. Such hydrogen-bond frameworks buffer the fluctuation of cell parameters and restrain molecular diffusion under an EEF. Increasing the electric field shortens the N-NO_2 trigger bond and reduces its interaction energy, strengthening the intrinsic sensitivity of CL-20 solvates. The conformers of CL-20 molecules transform from the α-phase to the stable ε phase after 0.4 V·Å^{-1}. When an external electric field acts on the CL-20/H_2O_2 and CL-20/H_2O energetic solvates, conformational changes in CL-20 molecules and solvation interactions can effectively reduce stiffness and enhance lattice ductility, reducing hotspot formation and thereby improving thermal safety.

Keywords: energetic solvates; external electric field; structural evolution

1. Introduction

Energetic materials, as a special type of fine chemical product, are widely used in gunpowder, explosives, propellants, and pyrotechnics, playing an important role in national defense and the national economy [1–3]. Their high nitrogen content and outstanding thermal stability make them have significant application potential in fields such as explosives and propellants. The study of the effects of external electric fields (EEFs) on the properties of energetic materials provides important guidance for designing and synthesizing new explosives that combine safety, thermal stability, and high-energy insensitivity. 2,4,6,8,10,12-hexanitro-2,4,6,8,10,12-hexacyclohexadecane (CL-20) is a currently outstanding cage-type nitramine explosive with excellent comprehensive performance, high energy density and detonation performance, whereas its application was limited by the high mechanical sensitivity. As a novel modification technology, energetic materials combine two or more different molecules through non-covalent bonds into the same lattice, forming a multi-component crystal with a specific structure and properties, such as reducing the sensitivity of explosives and improving the density, oxygen balance and thermal stability of explosives [4,5].

To reduce the mechanical sensitivity, some insensitive energetic materials were selected as ligands to form eutectics with CL-20, effectively enhancing their density, thermal

Check for updates

Academic Editor: Miguel A. Esteso

Received: 7 July 2026
Revised: 9 August 2026
Accepted: 10 August 2026
Published: 12 August 2026

Copyright: © 2026 by the authors. Licensee MDPI, Basel, Switzerland. This article is an open access article distributed under the terms and conditions of the Creative Commons Attribution (CC BY) license.

stability, and mechanical sensitivity [6–8]. In recent years, CL-20 has formed cocrystals with various compounds (both energetic and non-energetic), including the early CL-20/TNT and CL-20/HMX energetic cocrystals [9,10]. The Nitro-π interaction was performed on the electron-deficient ring of BTF in CL-20/BTF cocrystals, and its detonation performance was superior to that of BTF [11]. In 2016, the polymorphic form of CL-20/hydrogen peroxide (HP) energetic solvates (orthorhombic and monoclinic) were formed with a higher crystal density (respectively 2.03 and 1.96 g/cm^3) and higher detonation velocity and pressure, approaching the level of ε-CL-20, effectively improving the oxygen balance and thermal stability of CL-20 explosives [12]. Two new DNBT/hydrogen peroxide (HP) solvates are also similar to the above CL-20-based multi-component materials [13]. These materials employ multiple bonding modes with CL-20 and emphasize the importance of an in-depth understanding of weak intermolecular interactions, such as C-H···nitro, for the design of multi-component energetic substances, thereby confirming the potential of CL-20 as a universal cocrystal former.

The influence of temperature and pressure on the structure and properties of explosives has been comprehensively studied through theory and experiments [14–19]. However, theoretical research on energetic solids under external electric fields has not yet been carried out, although accidents caused by static electricity in explosive production plants easily occur, which is partly attributed to the fact that the influence of external electric fields on the structure and properties of energetic materials is still not fully understood. The effect of external electric fields on the sensitivity of explosives is analyzed by the molecular and electronic structure, the frontier molecular orbital energy gap, AIM electron density analysis and the electrostatic potential [20–22]. In 2015, the effect of external electric fields on the decomposition rate of crystalline lead azide using periodic first-principles calculations was explored [23]. The effect of external electric fields on the influence of energetic pentazole crystals on the energetic cocrystals at the molecular level, through parameters such as bond dissociation energy of N-NO_2, frontier molecular orbitals, electrostatic potential (ESP), and nitro group charge (Q_{NO2}), has also been studied [24,25]. Furthermore, the buffering mechanism of external electric fields on the initial thermal decomposition process of a series of chain-catenated Nx (x = 4, 8, 10) energetic crystals and energetic pentazole crystals has been elucidated using first-principles calculations [26,27]. In addition, Politzer et al. studied the effect of external electric fields on five typical trigger bonds, clarifying the type of bond breakage that plays a key role in detonation initiation [28]. The transfer of electrons and oxygen atoms in nitro groups is crucial in energetic material triggering reactions, and N-NO_2 is usually the trigger bond of nitramine explosives [29]. The influence of external electric fields on the bond dissociation energy and energy barrier of the trigger bonds of C-NO_2 or N-NO_2 bond in CH_3NO_2 or NH_2NO_2 and BITE-101 crystals was systematically studied [30,31]. However, studies on the sensitivity and other performance of CL-20-based energetic solvate cocrystals under electric fields are relatively rare, which hinders a deeper understanding of the decomposition mechanism of energetic materials under external electric fields.

In this work, the structural evolution and physical response of CL-20/H_2O_2 and CL-20/H_2O energetic solvates were studied under an EEF applied along the *z*-axis using molecular dynamics (MD) simulations, with intensities ranging from 0.0 to 1.4 V·Å^{-1}. Specifically, we analyze the gradient changes of crystal structure induced by an EEF, characterize the evolution of hydrogen bond networks via radial distribution functions, evaluate molecular mobility using root mean square displacement, explore the structural variations of the trigger bond (N-NO_2), and quantify the anisotropic changes in mechanical properties and cohesive energy density of the solvates. The primary objectives of this study are to reveal the regulatory mechanism of an EEF on the structure-property relationships of

CL-20-based solvates, clarify the differences in EEF response sensitivity between H_2O and H_2O_2 solvent systems, and provide theoretical references for the safety optimization and performance tailoring of EMs under extreme electromagnetic environments. This theoretical research contributes to a deeper understanding of the decomposition mechanisms of energetic materials under external electric fields and has significant implications for their use and storage in complex electromagnetic environments.

2. Results and Discussion

2.1. Crystal Structures and Conformers

To explore the effect of external electric fields on the conformational transformation of energetic solvate crystals, geometric relaxation of supercells was performed under different electric field intensities. All initial crystal configurations were derived from experimental low-temperature XRD data from the CCDC database and fully relaxed under ambient temperature and pressure, ensuring that all simulation models correspond to thermodynamically stable and experimentally conforming structures. The crystal structures of CL-20/H_2O_2 and CL-20/H_2O solvates are shown in Figure 1. The electric field is applied along the positive crystallographic *z*-axis of optimized supercells with MD simulations, which is parallel to the orientation of N-NO_2 trigger bonds of CL-20 inside the crystal lattice.

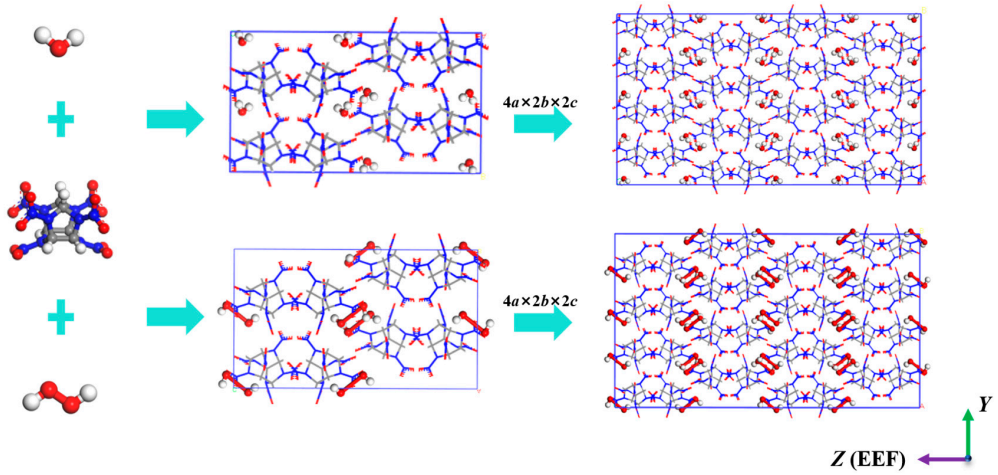


Figure 1. Unit cells and supercells of CL-20/H_2O_2 and CL-20/H_2O energetic solvates. The crystal orientation relative to the applied electric field (*z*-axis) is indicated at the bottom-right corner.

Figure 2 shows the variations in lattice parameters, unit-cell volume, and density of the CL-20/H_2O_2 and CL-20/H_2O solvates as a function of the applied electric field. For CL-20/H_2O_2, the lattice parameters a, b, and c initially increase with the field strength rising from 0.0 to 0.4 V/Å, plateau at 0.4–0.6 V/Å, and then decrease gradually. The unit-cell volume V also rises rapidly to a maximum in this range. As the field increases from 0.6 to 1.4 V/Å, the lattice parameters and volume decrease gradually, while the density increases slowly.

In contrast, the lattice parameters and density of CL-20/H_2O (α-CL-20) first increase monotonically and then decrease over 0.0–1.4 V/Å. The amplitude of variation is significantly larger, indicating that the structure of CL-20/H_2O is more sensitive to electric-field-induced polarization. This difference can be attributed to their distinct stoichiometries and crystal structures. CL-20/H_2O_2 crystallizes in the P_{bca} space group with a 2:1 stoichiometry and eight CL-20 molecules per unit cell, while CL-20/H_2O has a 4:1 stoichiometry with two solvent molecules in the unit cell. The higher solvent content in CL-20/H_2O_2 enhances intermolecular interactions, stabilizes the crystal lattice, and buffers the structural deformation under external electric fields.

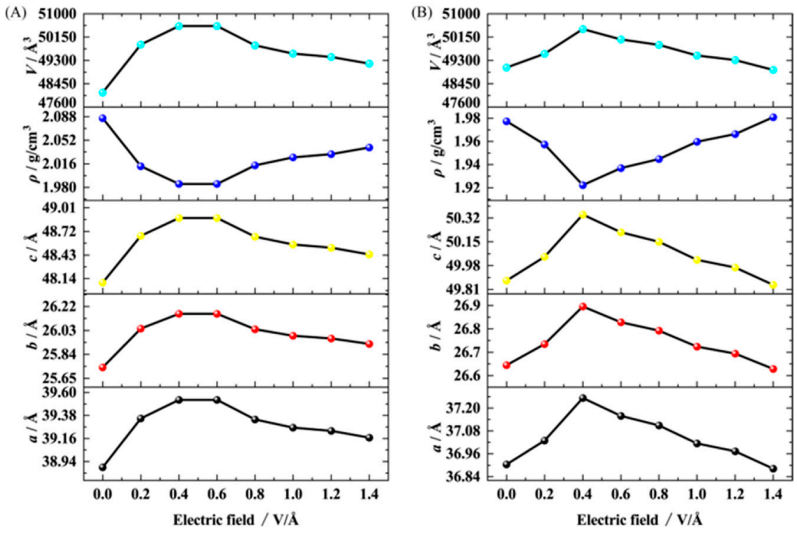


Figure 2. The variation for lattice parameters, volume, and density of (**A**) CL-20/H_2O_2 and (**B**) CL-20/H_2O solvates under increased external electric fields applied along the *z*-axis.

The difference in lattice stability mentioned above is essentially determined by the type of solvent guest molecules. CL-20-based energetic solvates were formed by substituting H_2O molecules in the CL-20/H_2O solvate (α-CL-20) with hydrogen peroxide. This breakthrough enables the cocrystallisation of small oxygen-containing molecules without sacrificing the energy level of the explosives. The CL-20 at different temperatures and pressures has been investigated with α, β, ε, and γ based on the difference in the initial orientation of the nitro group in the molecule and lattice packing, whose stability order is ε > γ > α > β [32–35]. The molecular structures of the four CL-20 polymorphs are shown in Figure 3A. Figure 3B,C show the structural evolution of CL-20/H_2O_2 and CL-20/H_2O solvates under varying intensities of the external electric field applied along the *z*-axis. The results reveal that the space orientation of the NO_2 groups of CL-20 in CL-20/H_2O_2 and CL-20/H_2O solvates changes with increasing field strength and transforms into the stable ε conformers after 0.4 V·Å^{-1}. It is due to changes in the orientation of the CL-20 molecular dipole moment induced by electric-field interactions between CL-20 molecules, as well as alterations in the chemical environment from solvent effects, which in turn lead to conformational changes.

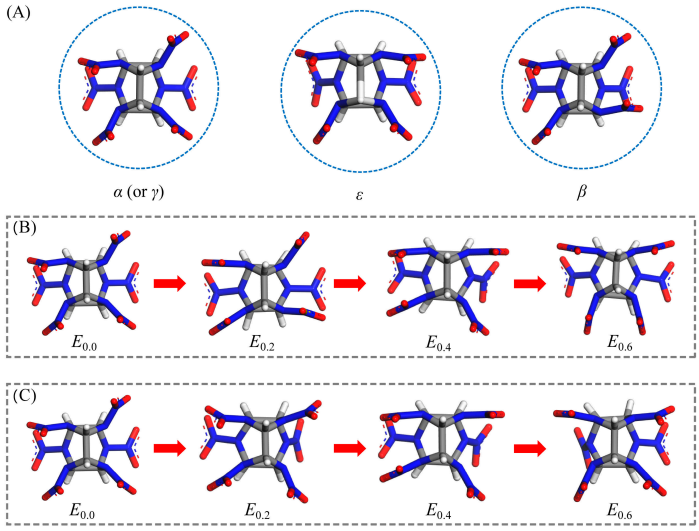


Figure 3. (**A**) The conformers of CL-20 molecules. (**B**) The conformer evolution of CL-20/H_2O_2 and (**C**) CL-20/H_2O solvates under different intensities of external electric fields.

2.2. Intermolecular Interactions Analysis

Generally, radial distribution function (RDF) analysis can be used to measure local spatial ordering by providing the probability density g(*r*) of finding an atom at a distance *r* from a reference atom. Generally, the interaction distance range (*r*) for the hydrogen bond is 2.0–3.1 Å, and for strong van der Waals, it is 3.1–5.0 Å. The van der Waals (vdW) interactions become negligible beyond 5.0 Å [5]. Figure 4 shows the RDFs of O···H or O···O atomic pairs in CL-20/H_2O_2 and CL-20/H_2O solvates under the increased electric field intensities. Here, two typical intermolecular hydrogen-bond configurations are defined as H (H_2O_2 or H_2O)···O(CL-20) (solvent as H-donor, CL-20 nitro oxygen as H-acceptor) and O (H_2O_2 or H_2O)···H(CL-20) (solvent oxygen as H-acceptor, CL-20 C-H as H-donor). The O···O contact between CL-20 and solvent molecules originates from intermolecular dipole electrostatic attraction between neutral molecules. No ionic dissociation of hydrogen or oxygen atoms is observed under external electric field. In Figure 4, the first intense peaks of the RDFs for H···O/O···H atom pairs in CL-20/H_2O_2 are located at 1.69 and 2.41 Å, which are shorter than the corresponding first peaks of H···O/O···H atoms pairs in CL-20/H_2O (1.73 and 2.59 Å), respectively. In addition, the primary O···O atom pair peaks of both CL-20/H_2O_2 and CL-20/H_2O solvates appear at 2.69 Å. These results reveal that intermolecular hydrogen bonding serves as the dominant interaction between CL-20 and solvent molecules, accompanied by van der Waals interactions. Moreover, the hydrogen-bonding interaction between CL-20 and H_2O_2 is stronger than that between CL-20 and H_2O, where H_2O_2 molecules provide hydrogen bond donors.

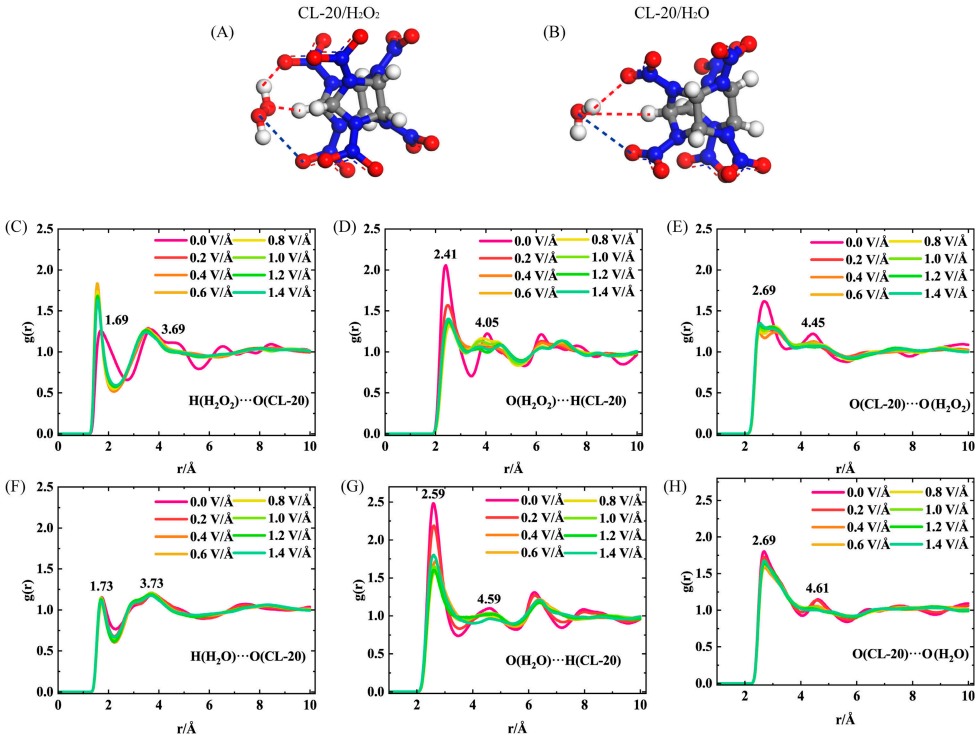


Figure 4. The extracted interaction pairs of O···H or O···O atoms (**A**,**B**). Radial distribution functions (RDFs) of special atom pairs in CL-20/H_2O_2 (**C**–**E**) and CL-20/H_2O solvates (**F**–**H**).

In addition, based on the QTAIM (Quantum Theory of Atoms in Molecules) [36,37], the more detailed information about the hydrogen-bonding interactions can be obtained by conducting topological analyses on the molecular clusters extracted from the CL-20/H_2O_2 and CL-20/H_2O solvates (seen from Figure S2). Table S1 present the topological parameters of the hydrogen bonds in the CL-20/H_2O_2 and CL-20/H_2O solvates, respectively. The electron density (ρ) and its Laplacian ($\nabla^2\rho$) are two important parameters to quantify the

interactions strength. The criterion for the existence of non-bonding interactions at the critical point is that the closed-shell interaction ρ is less than 0.1 a.u. and $\nabla^2\rho$ possesses a small and positive value. The values of ρ and $\nabla^2\rho$ at the bond critical points (BCPs) of CL-20/H_2O_2 range from 0.0161 to 0.0137 a.u. and 0.0454 to 0.0466 a.u., respectively, while those for CL-20/H_2O from 0.0105 to 0.0121 a.u. and 0.0406 to 0.0489 a.u. It confirms that these bond critical points between O and H atoms represent the hydrogen bonds. The values of Eb of CL-20/H_2O_2 and CL-20/H_2O are from 10.35 to 11.25 kJ mol^{-1} and 9.86 to 10.83 kJ mol^{-1}, suggesting these hydrogen bond of between O and H atoms in CL-20/H_2O_2 are stronger than those in CL-20/H_2O. The above RDF qualitative comparison combined with QTAIM quantitative topological analysis jointly verify the intrinsic difference in intermolecular interaction strength between the two solvates.

Subsequently, the effect of external electric field strength on the intermolecular H···O and O···O atom pairs is discussed. Figure 5 presents the variations of g(*r*) and *r* of H···O and O···O interactions in the solvated complexes of CL-20/H_2O_2 and CL-20/H_2O with the electric field strength. The distance between the intermolecular H···O atom pairs at 1.69 Å and the O···O interaction atoms at 2.69 Å in CL-20/H_2O_2 is shortened after applying an electric field, while the distance of atom pairs in the CL-20/H_2O solvate remains almost unchanged, indicating that the intermolecular interactions between CL-20/H_2O_2 molecules are more sensitive to the influence of the electric field. In addition, the shortening of RDF gradually disappears at 0.4 V/Å, indicating that the electric field strength of 0.4 V/Å is the turning point for the structural changes of CL-20 based solvates, which are also more sensitive to CL-20/H_2O_2 solvates with electric field strength (Figure 5A,B).

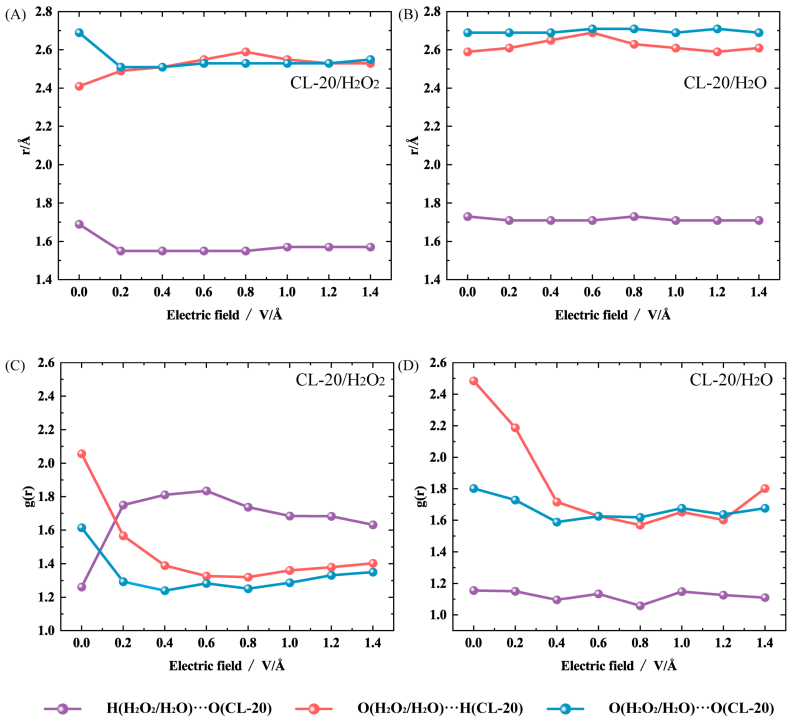


Figure 5. The variation of g(r) and r of CL-20/H_2O_2 (**A**,**C**) and CL-20/H_2O (**B**,**D**) solvates with an external electric field applied along the *z*-axis.

2.3. Mean Square Displacement (MSD)

The mean-square displacement (MSD) and diffusion coefficient (D) are calculated by analyzing molecular dynamic trajectories under applied electric fields, as illustrated in Figure 6. Figure 6A,B reveal that the H_2O molecule inside the CL-20-based energetic solvate exhibits a relatively larger MSD value. The diffusion coefficient fluctuates remark-

ably with electric field intensity, showing an upward trend followed by a decline and peaking at 0.4 V/Å. CL-20/H_2O and CL-20/H_2O_2 share identical variation tendency of diffusion coefficient with the maximum value obtained at 0.4 V/Å, demonstrating that the intermolecular interaction between CL-20 and solvent molecules undergoes obvious transition at this electric field. The larger diffusion coefficient indicates faster diffusion of molecules or atoms. Compared with the CL-20/H_2O_2 solvates, CL-20/H_2O is more susceptible to the influence of field strength changes. Moreover, the H_2O molecules in α-CL-20 possess a higher diffusion rate than H_2O_2 molecules. This further indicates that the interaction between CL-20 and H_2O_2 molecules is stronger, and the stability of the crystal lattice is enhanced.

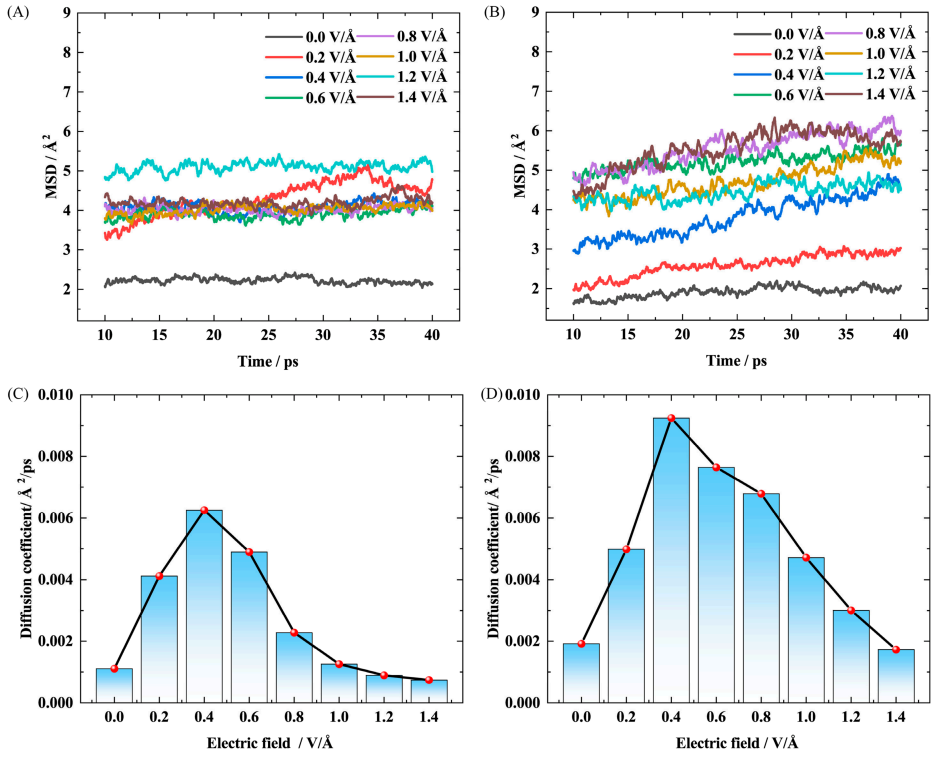


Figure 6. The mean square displacement and diffusion coefficient of CL-20/H_2O_2 (**A**,**C**) and CL-20/H_2O (**B**,**D**) solvates with an external electric field applied along the *z*-axis.

2.4. The Interaction Energy of the Trigger Bond

Based on the hot-spot theory, the trigger bond is the weakest chemical bond in energetic materials and the most likely to break when exposed to external stimuli, thereby causing the explosive to decompose or explode. Here, the maximum length and the interaction energy of the trigger bond (denoted as $E_{N\text{-}N}$ in the N-NO_2 bond) were selected in CL-20-based energetic solvates as practical indicators for predicting explosive sensitivity. The statistical distribution of trigger bond lengths offers fundamental insights into the stability and safety of explosives. A lower $E_{N\text{-}N}$ correlates with a weaker trigger bond, facilitating the initiation of decomposition or detonation. The expression of $E_{N\text{-}N}$ is as follows:

$$E_{N-N} = \frac{E_1 - E_2}{n} \quad (1)$$

where E_1 represents the total energy of the system in its thermodynamic equilibrium state and E_2 is the total energy of the system when it reaches equilibrium after fixing the three-dimensional coordinates of all N atoms in CL-20. For the CL-20, All N atoms constitute the cage skeleton of CL-20 and participate in forming N-NO_2 trigger bonds. By comparing

E_1 and E_2, we can obtain the intrinsic interaction energy of the N-NO_2 trigger bond, and this calculation strategy can effectively eliminate the energy perturbations originating from lattice vibration and structural deformation. n is the number of N-NO_2 bonds in the cocrystal system.

The interaction energy of the trigger bond ($E_{N\text{-}N}$) for is shown in Figure 7. Notably, $E_{N\text{-}N}$ of the trigger bond N-NO_2 shows a trend of initial decrease and subsequent gradual increase with the increase of the EEF. Under no electric field, the value of $E_{N\text{-}N}$ of CL-20/H_2O_2 and CL-20/H_2O are 182.58 kJ/mol and 180.95 kJ/mol, respectively. Under the EEF at 0.4 V/Å, the $E_{N\text{-}N}$ decreases to varying extents and reaches the minimum, where CL-20/H_2O_2 and CL-20/H_2O are respectively at 176.51 kJ/mol and 177.45 kJ/mol. Further, CL-20/H_2O_2 exhibits a larger reduction of $E_{N\text{-}N}$, which demonstrates that H_2O_2 molecules amplify the structural perturbation of the EEF on CL-20 and render the solvate more sensitive under electric field environment. As the electric field rises from 0.4 to 1.4 V/Å, the interaction energy of the trigger bond gradually rebounds. This behavior is attributed to the enhanced molecular polarity and lattice contraction, which restrict the structural deformation and dissociation of the N-NO_2 trigger bond and moderately improve bond stability.

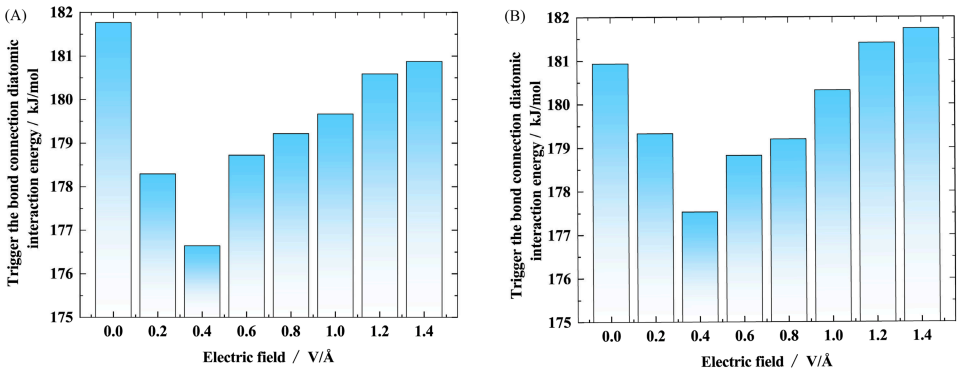


Figure 7. The interaction energy of the trigger bond ($E_{N\text{-}N}$) for CL-20/H_2O_2 (**A**) and CL-20/H_2O (**B**) solvates with an external electric field applied along the *z*-axis.

Nevertheless, the $E_{N\text{-}N}$ values under the EEF are all lower than the zero-field system overall, the positive *z*-direction electric field weakens the N-NO_2 trigger bond and the $E_{N\text{-}N}$, and the molecular sensitivity increases. The reduction of $E_{N\text{-}N}$ of the trigger bond N-NO_2 originates from the directional perturbation of electric fields on the intermolecular hydrogen bond network and van der Waals interactions, which irreversibly disturbs the molecular stacking and dipole arrangement of CL-20 and guest molecules.

This is consistent with previous reports on the electric field response of CL-20/H_2O_2 solvates [38], where H_2O_2 accelerates the transformation of the CL-20 skeleton structure and weakens adjacent C-N chemical bonds due to the swinging of nitro groups, thereby reducing the stability of CL-20 and improving system sensitivity. This can be explained by the fact that H_2O_2 and the hydroxyl radicals (OH·) generated from its decomposition promote the destruction of the cage-like skeleton of CL-20 by reactive force field molecular dynamics simulations (ReaxFF RMD simulation), while generating a large number of water molecules and releasing heat. Therefore, the decomposition rate of CL-20/H_2O_2 is higher than that of ε-CL-20.

Figure 8 displays the distributions of bond lengths of the N-NO_2 trigger bond of CL-20/H_2O_2 and CL-20/H_2O solvates in the equilibrium system obtained from MD simulation. The bond length distribution presents an approximately symmetrical Gaussian distribution, suggesting that their most probable bond length (L_{prob}) is consistent with the average bond length (L_{ave}). The bond length of N-NO_2 in CL-20/H_2O_2 and CL-20/H_2O is 1.39 Å in the

absence of an external electric field, which is close to the experimental value (the bond length of N-NO_2 in ε-CL-20 is 0.138 nm) [25].

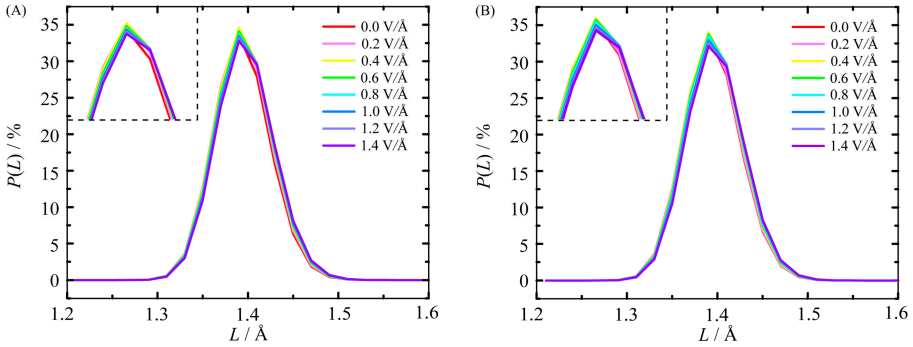


Figure 8. The trigger bond length distribution of CL-20/H_2O_2 (**A**) and CL-20/H_2O (**B**) solvates.

With the increase of positive z-direction external electric field strength, the distribution of N-NO_2 bond lengths in all crystals gradually narrows and shifts towards the shorter bond lengths. This indicates obvious geometric contraction of the trigger bond under electrostatic polarization. Notably, significant structural variation occurs at 0.4 V/Å, which corresponds to the critical conformational transition point of the CL-20 solvate systems.

2.5. Cohesive Energy Density

Cohesive energy density (CED) quantitatively characterizes the strength of the intermolecular interactions within a crystal. Figure 9 presents the cohesive energy density of the CL-20/H_2O_2 and CL-20/H_2O solvates at 0.0 V/Å to 1.4 V/Å, together with the separate contributions from van der Waals forces and electrostatic forces. Under different electric field intensities, the cohesive energy density of CL-20/H_2O_2 is consistently greater than that of CL-20/H_2O. When the electric field intensity is below 0.4 V/Å, the CED decreases as the electric field intensity increases. When the electric field intensity exceeds 0.4 V/Å, the cohesive energy density of CL-20/H_2O_2 increases and stabilizes, and is predominantly governed by electrostatic interactions. In contrast, the CED of CL-20/H_2O decreases continuously as the electric field intensity increases, which mainly originates from the weakening of electrostatic forces. This further indicates that hydrogen bonding is the primary intermolecular driving force in CL-20-based solvates, and that the interaction between CL-20 and H_2O_2 molecules is more stable.

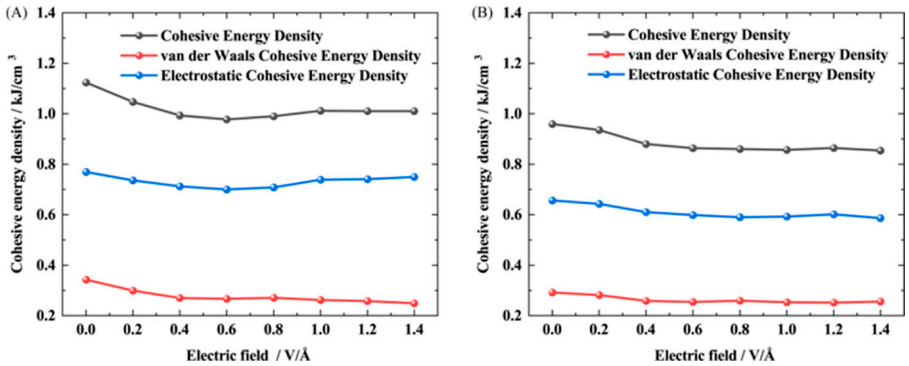


Figure 9. Cohesive energy density (CED) of CL-20/H_2O_2 (**A**), CL-20/H_2O (**B**) solvates with an external electric field applied along the *z*-axis.

Although the external electric field compresses the N-NO_2 bond geometry, the reduced trigger bond interaction energy under all applied electric fields and the continuous decline in cohesive energy density demonstrate that the positive EEF generally weakens both

intramolecular trigger bonding and intermolecular interactions. Accordingly, the geometric contraction of the N-NO_2 bond cannot independently improve the overall stability of CL-20-based energetic solvates. Therefore, it also reflects that the trigger bond shortening is merely a geometric feature rather than reliable evidence of improved structural stability.

2.6. Mechanical Properties

Mechanical properties are one of the most critical indicators of energetic materials characterization [22]. Three mechanical parameters including elastic stiffness constants, engineering moduli and Poisson's ratio were calculated, with elastic constants describing the intrinsic stress–strain relationship of the crystalline materials. Figure 10 summarizes the evolution of the elastic constants of CL-20/H_2O_2 and CL-20/H_2O solvates under the external electric field. The diagonal elements of the elastic constant tensor exhibit obvious anisotropic mechanical responses in CL-20-based solvates. Comparing the elastic constants C11, C22, and C33 at 298 K and 101 kPa, CL-20/H_2O_2 solvate possesses superior shear thermal stability. The elastic constants of CL-20/H_2O_2 solvates increase continuously with the electric field loading apart from along the b-axis.

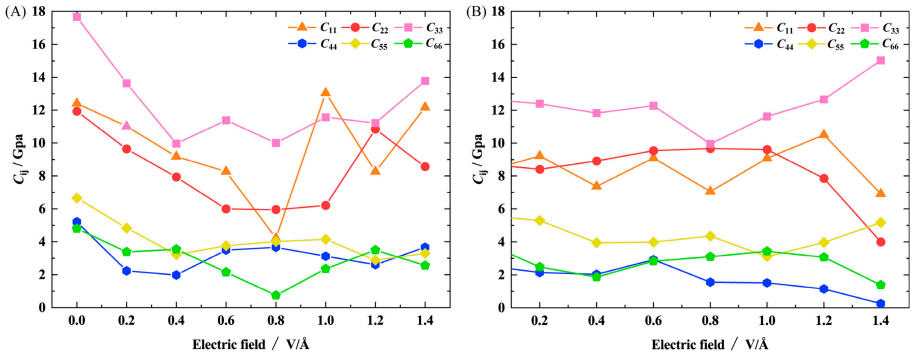


Figure 10. The elastic coefficients of CL-20/H_2O_2 (**A**) and CL-20/H_2O (**B**) solvates under different external electric fields applied along the *z*-axis.

For CL-20/H_2O, elastic constants remain stable at a low electric field and fluctuate markedly at high field strength. The elastic coefficient of the *a*- and *b*-axis decreases but that of the c-axis increases with the EEF. This indicates that CL-20/H_2O solvates are more sensitive to external electric-field regulation and can be used as an effective means to reduce their elastic constants. This is also related to the stronger intermolecular hydrogen bonding in CL-20/H_2O_2, which stabilizes the crystal structure. Once the external electric field exceeds the critical value at the conformational transition point, the variation amplitude of elastic coefficients is significantly enlarged, which confirms the regulatory effect of the external electric field on the structure of CL-20-based solvated species.

Engineering moduli are used to characterize the rigidity and elastic deformation resistance of energetic crystals. Young's modulus (E) and shear modulus (G) directly reflect structural rigidity, with larger values corresponding to stiffer crystals. Bulk modulus (B) is adopted to evaluate compressive fracture resistance, calculated by averaging the Voigt and Reuss bounding values; a higher bulk modulus indicates stronger anti-fracture capacity. Young's modulus E and Poisson's ratio γ can be derived from bulk modulus B and shear modulus G via the following formulas [39]:

$$E = 2G(1+\gamma) = 2B(1-2\gamma) \quad (2)$$

$$\gamma = \frac{3B-2G}{2(3B+G)} \quad (3)$$

Tables 1 and 2 list the Young's modulus E, bulk modulus B, shear modulus G, Poisson's ratio γ, and B/G of CL-20/H_2O_2 and CL-20/H_2O solvates under different external electric field. Figure 11 presents mechanical performance parameters of CL-20/H_2O_2 and CL-20/H_2O solvates under different external electric field applied along the z-axis. Relative to the zero-field state, E, B, and G of the two CL-20-based solvates show an overall decrease under the electric field, except at 1.0 V/Å for CL-20/H_2O solvates. This demonstrates that z-axis directional electric field weakens the overall structural rigidity of CL-20 energetic solvates. Furthermore, the modulus fluctuation range of CL-20/H_2O is far larger than that of CL-20/H_2O_2, indicating the rigidity of CL-20/H_2O is more susceptible to electric field disturbance.

Table 1. Mechanical properties of CL-20/H_2O_2 solvates under different electric fields.

Modulus	0.0 V/Å	0.2 V/Å	0.4 V/Å	0.6 V/Å	0.8 V/Å	1.0 V/Å	1.2 V/Å	1.4 V/Å
E	12.06	7.24	5.73	4.59	3.90	3.59	4.23	3.72
B	8.09	7.49	6.47	6.37	5.34	4.95	5.25	5.12
G	4.82	2.70	2.12	1.67	1.41	1.30	1.51	1.33
K/G	1.68	2.77	3.06	3.83	3.78	3.81	3.48	3.84
γ	0.25	0.34	0.35	0.38	0.38	0.38	0.40	0.39
C_{12}–C_{44}	−1.78	4.29	3.33	2.03	2.49	5.26	3.92	2.65

Table 2. Mechanical properties of CL-20/H_2O solvates under different electric fields.

Modulus	0.0 V/Å	0.2 V/Å	0.4 V/Å	0.6 V/Å	0.8 V/Å	1.0 V/Å	1.2 V/Å	1.4 V/Å
E	7.84	6.84	6.69	6.41	5.34	7.37	6.34	6.95
B	6.09	6.40	6.57	7.32	5.34	4.95	7.06	5.86
G	3.34	2.67	2.23	2.10	1.16	2.22	1.11	1.31
B/G	1.82	2.40	2.95	3.48	4.62	2.23	6.36	4.49
γ	0.29	0.32	0.37	0.36	0.30	0.30	0.36	0.34
C_{12}–C_{44}	2.78	3.76	3.96	3.80	4.68	4.75	3.98	4.62

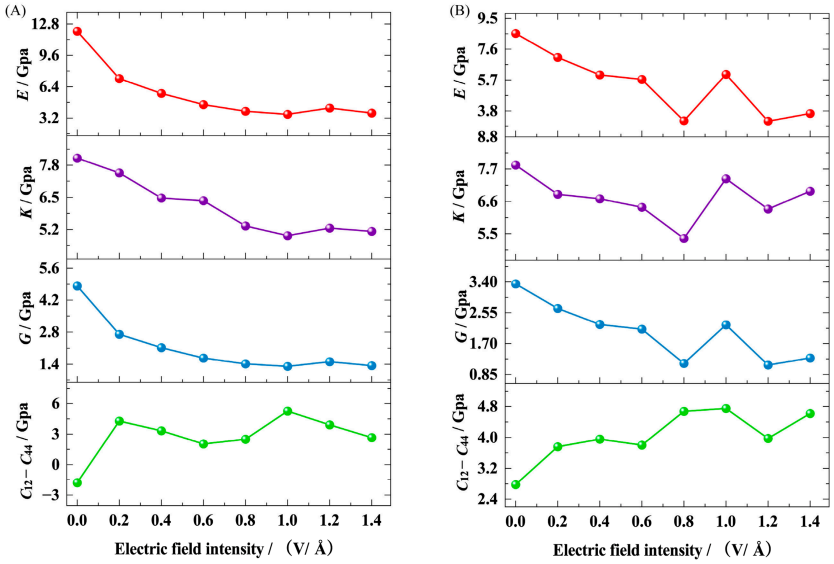


Figure 11. Mechanical performance parameters of CL-20/H_2O_2 (**A**) and CL-20/H_2O (**B**) solvates under different external electric fields applied along the z-axis.

Poisson's ratio (γ) is a typical indicator for crystal plastic deformation, with a typical range of 0.2–0.4 for condensed crystals. External electric field markedly elevates the

Poisson's ratio of both solvates. As listed in Tables 1 and 2, the Poisson's ratio of CL-20/H_2O_2 rises from 0.25 to 0.39, while that of CL-20/H_2O increases from 0.28 to 0.31. The elevated Poisson's ratio reveals enhanced plastic deformation capacity and larger elastic elongation under electric field loading. The *B/G* ratio is another ductility-brittleness discriminant: a higher *B/G* value corresponds to better ductility. The *B/G* values of both CL-20 solvates increase significantly under electric field excitation. In conclusion, the external electric field effectively improves the plastic ductility of energetic solvate crystals.

Cauchy pressure (C_{12}–C_{44}) is widely used to judge the ductility or brittleness of energetic crystals: positive Cauchy pressure represents ductile behavior, whereas negative value means brittle characteristic. The Cauchy pressure of both crystals increases monotonically with rising electric field intensity. At ambient conditions (298 K, 101 kPa) without electric field, CL-20/H_2O_2 behaves as brittle with negative Cauchy pressure, while pristine CL-20/H_2O shows intrinsic ductility. The ductility of both solvate crystals is greatly strengthened under the electric field. This result confirms that the external electric field suppresses crystal brittleness and improves ductility efficiently.

3. Materials and Methods

The crystal structures of CL-20/H_2O_2 and CL-20/H_2O solvates were obtained by X-ray diffraction from the Cambridge Crystallographic Database v6 (CCDC, Cambridge, UK). The unit cells of CL-20/H_2O_2 and CL-20/H_2O solvates are enlarged along 4a × 4b × 2c three directions to gain the supercells of CL-20/H_2O_2 (5120 atoms) and 4a × 4b × 2c CL-20/H_2O (4992 atoms).

In addition, some other studies [24,25] have shown that the EEF has a significant effect on the trigger bond when it is parallel to the trigger bond. In this work, the structural optimization and Laplacian bond order (LBO) analysis were performed at the 6-311G++(d, p) basis set level using the B3LYP method [40], and wave function information was calculated using the Gaussian 09 program [41], imported into Multiwfn 3.8 [42,43] and VMD v1.9.3 [44] was used for analysis. According to the result of Laplacian bond order calculation (Figure S1), the N-NO_2 bond was selected as the trigger bond. Among six spatially distinct N-NO_2 bonds of the CL-20 cage, the trigger bond with the lowest bond order was selected as the characteristic bond. VMD was adopted to rotate the crystal configuration to align this specific N-NO_2 bond parallel to the *z*-axis, and the positive z-direction was defined as the positive direction of the applied electric field. The same orientation strategy was applied to the CL-20/H_2O and CL-20/H_2O_2 solvates for consistent comparison. The external electric field was applied along the *z*-axis with a range from 0.0 to 1.4 V·Å^{-1}, with an interval of 0.2 V·Å^{-1}.

Geometry optimization was performed to minimize interatomic contacts using the COMPASSII force field, which has been validated for ammonium nitrate energetic materials containing H, O, and N atoms [45]. Then, the optimized structures were equilibrated under the NPT ensemble at 298 K and 0 GPa for a total of 200 ps with 0.1 fs time steps, and the system was sufficiently relaxed, as indicated by the fluctuation profiles of temperature and energy. Then, MD simulations were performed under the NPT ensemble with a total simulation time of 500 ps and a time step of 0.1 fs. The Berendsen thermostat and barostat were employed to maintain the temperature and pressure at 298 K and 0 GPa, respectively, with decay constants of 0.1 ps for both. Van der Waals interactions were computed using the atom-based summation method with a long-range correction and a cutoff distance of 15.5 Å. Electrostatic interactions were evaluated using the Ewald summation method with a buffer width of 0.5 Å and an accuracy of 0.001. The mean-squared displacement (MSD) is analyzed for the first 300 ps of motion trajectories of solvent molecules in energetic solvates, and the diffusion coefficient (*D*) is then calculated from the resulting MSD [46]. All MD

simulations under external electric fields were conducted using the Forcite Module and Perl scripts in Materials Studio 8.0.

4. Conclusions

In this work, theoretical simulations were conducted to explore the structural evolution, intermolecular interaction, trigger bond stability, sensitivity and mechanical properties of CL-20/H_2O_2 and CL-20/H_2O solvates under a *z*-axis external electric field (EEF). Compared with CL-20/H_2O, CL-20/H_2O_2 solvates possess stronger intermolecular O-H···O/C-H···O hydrogen bonds. The hydrogen bond networks can buffer the variation of cell parameters under external electric field, suppress molecular diffusion and decrease the interaction energy of the trigger bond of N-NO_2 ($E_{N\text{-}N}$) and cohesive energy density (CED). The conformers of CL-20 molecules transform from the α-phase to the thermodynamically stable ε phase after 0.4 V·Å^{-1}, suggesting that the orientation of the NO_2 groups is adjustable and that the phase transition occurs under the applied field. The reduced stiffness and enhanced lattice ductility of mechanical properties enables effective buffering and uniform dispersion of external stress through conformational rearrangement of CL-20 molecules and flexible solvation interactions. This suppresses hotspot generation and improves the thermal safety of energetic crystals under impact loading. This work reveals the electric response mechanism at the molecular level of CL-20 solvates and provides theoretical guidance for electric-field modification.

Supplementary Materials: The following supporting information can be downloaded at: https://www.mdpi.com/article/10.3390/ijms27167209/s1.

Author Contributions: Conceptualization, methodology, writing—original draft, and project administration, L.S.; data curation and funding acquisition, L.F. and H.S.; software and resources, D.M. All authors have read and agreed to the published version of the manuscript.

Funding: This work was supported by the start-up fund at Mianyang Teachers' College (no. QD2022A06) and the college students' innovative entrepreneurial training plan program in Sichuan province (S202510539007, S202510639011, S202610639004).

Institutional Review Board Statement: Not applicable.

Informed Consent Statement: Not applicable.

Data Availability Statement: The original contributions presented in this study are included in the article. Further inquiries can be directed to the corresponding author.

Conflicts of Interest: The authors declare no conflicts of interest.

References

1. Meng, L.; Song, Q.G.; Yao, C.; Zhang, L.; Pang, S.P. Chemical reaction mechanisms and models of energetic materials: A perspective. *Energ. Mater. Front.* **2025**, *6*, 129–144. Correction in *Energ. Mater. Front.* 2026, *in press*. [CrossRef]
2. Yadav, A.K.; Dharavath, S. Shaping the future of energetic materials: Breakthroughs, barriers, and emerging frontiers. *Chem. Commun.* **2025**, *61*, 16547–16559. [CrossRef] [PubMed]
3. Zhong, K.; Zhang, C.Y. Review of the decomposition and energy release mechanisms of novel energetic materials. *Chem. Eng. J.* **2024**, *483*, 149202. [CrossRef]
4. Liu, G.; Bu, R.; Huang, X.; Zhong, K.; Jiao, F.; Wei, S.-H.; Li, H.; Zhang, C. Energetic cocrystallization as the most significant crystal engineering way to create new energetic materials. *Cryst. Growth Des.* **2022**, *22*, 954–970. [CrossRef]
5. Lyu, R.Q.; Wei, Y.; Chen, J.; Zhong, K.; Wang, R.; Mou, C.L.; Wang, L.Y.; Huang, Z.Y.; Deng, H.B. Exploration for the optical properties and fluorescent prediction of nitrotriazole and nitrofurazan: First-principles and TD-DFT calculations. *ACS Omega* **2022**, *23*, 19694–19705. [CrossRef] [PubMed]
6. Bennion, J.C.; Matzger, A.J. Development and evolution of energetic cocrystals. *Acc. Chem. Res.* **2021**, *54*, 1699–1710. [CrossRef] [PubMed]

7. Anderson, S.R.; Dubé, P.; Krawiec, M.; Salan, J.S.; Ende, D.J.A.; Samuels, P. Promising CL-20-based energetic material by cocrystallization. *Propellants Explos. Pyrotech.* **2016**, *41*, 783–788. [CrossRef]
8. Bellas, M.K.; Matzger, A.J. Achieving balanced energetics through cocrystallization. *Angew. Chem. Int. Ed.* **2019**, *58*, 17185–17188. [CrossRef] [PubMed]
9. Bolton, O.; Simke, L.R.; Pagoria, P.F.; Matzger, A.J. High power explosive with good sensitivity: A 2:1 cocrystal of CL-20:HMX. *Cryst. Growth Des.* **2012**, *12*, 4311–4314. [CrossRef]
10. Zhang, X.-Q.; Yuan, J.-N.; Selvaraj, G.; Ji, G.-F.; Chen, X.-R.; Wei, D.-Q. Towards the low-sensitive and high-energetic co-crystal explosive CL-20/TNT: From intermolecular interactions to structures and properties. *Phys. Chem. Chem. Phys.* **2018**, *20*, 17253–17261. [CrossRef] [PubMed]
11. Yin, Y.; Wang, J.; Chen, J.; Sun, J.; Sui, H. Thermal kinetics of energetic CL-20/BTF cocrystal induced by strong intermolecular coupling. *J. Phys. Chem. C* **2022**, *126*, 8199–8207. [CrossRef]
12. Bennion, J.C.; Chowdhury, N.; Kampf, J.W.; Matzger, A.J. Hydrogen peroxide solvates of 2,4,6,8,10,12-hexanitro-2,4,6,8,10,12-hexaazaisowurtzitane. *Angew. Chem. Int. Ed.* **2016**, *55*, 13118–13121. [CrossRef] [PubMed]
13. Wiscons, R.A.; Bellas, M.K.; Bennion, J.C.; Matzger, A.J. Detonation performance of ten forms of 5,5′-dinitro-2H,2H′-3,3′-bi-1,2,4-triazole (DNBT). *Cryst. Growth Des.* **2018**, *18*, 7701–7707. [CrossRef]
14. Sun, X.; Liang, W.; Li, X.; Mai, D.; Zhang, Y.; Sui, Z.; Dai, R.; Zheng, X.; Wang, Z.; Duan, X.; et al. Structural evolution of CL-20/DNB cocrystals at high temperature: Phase transition and kinetics of thermal decomposition. *Spectrochim. Acta A* **2023**, *292*, 122436. [CrossRef] [PubMed]
15. Liang, W.; Sun, X.; Wang, H.; Wang, J.; Sui, Z.; Ren, H.; Dai, R.; Zheng, X.; Wang, Z.; Duan, X.; et al. Isothermal structural evolution of CL-20/HMX cocrystals under slow roasting at 190 °C. *Phys. Chem. Chem. Phys.* **2023**, *25*, 15756–15766. [CrossRef] [PubMed]
16. Chen, P.-Y.; Zhang, L.; Zhu, S.-G.; Cheng, G.-B. Theoretical study of BTF/TNA cocrystal: Effects of hydrostatic pressure and temperature. *Def. Technol.* **2015**, *11*, 132–139. [CrossRef]
17. Ndengué, S.; Quintas-Sánchez, E.; Dawes, R.; Blackstone, C.C.; Osborn, D.L. Temperature dependence of the electronic absorption spectrum of NO2. *J. Phys. Chem. A* **2023**, *127*, 6051–6062. [CrossRef] [PubMed]
18. Xie, Z.-M.; Wang, T.-W.; Kuang, B.-L.; Zhang, C.; Zhang, J.-G. Pressure-induced hydrogen bonds reconstruction of energetic material 3,6-dihydrazino-1,2,4,5-tetrazine: A DFT study. *Chem. Phys. Lett.* **2023**, *824*, 140572. [CrossRef]
19. Peng, H.; Jin, B.; Guan, J.; Luo, L.; Huang, T.; Peng, R. Isothermal decomposition of CL-20 before and after thermally induced ε-γ crystal transformation. *Mater. Sci. Eng. B* **2022**, *285*, 115941. [CrossRef]
20. Zhang, R.; Zhao, M.; Xia, W.; Ma, P.; Ma, C. Regulation of external electric field on sensitivity of ICM energetic materials. *J. Mol. Model.* **2023**, *29*, 62. [CrossRef] [PubMed]
21. Chen, J.; Xu, J.; Xiao, T.; Gao, Z.; Bo, M.; Gu, Z.; Ma, P.; Ma, C. The regulation of high-energy insensitive compound 2,6-diamino-3,5-dinitropyrazine-1-oxide by external electric field. *J. Mol. Model.* **2024**, *30*, 83. [CrossRef] [PubMed]
22. Du, J.; Wang, B.; Chen, Y.; Li, X.; Wang, C. Theoretical investigation of potential energetic material CL-20/TNBP co-crystal explosive based on molecular dynamics method. *J. Mol. Model.* **2024**, *30*, 348. [CrossRef] [PubMed]
23. Li, Z.; Huang, H.; Zhang, T.; Xu, J.; Zhang, J.; Yang, L. Electric-field-induced structural and electronic changes and decomposition of crystalline lead azide: A computational study. *J. Phys. Chem. C* **2015**, *119*, 8431–8437. [CrossRef]
24. Hao, L.; Wang, J.; Zhai, D.; Ma, P.; Ma, C.; Pan, Y.; Jiang, J. Theoretical study on CL-20-based cocrystal energetic compounds in an external electric field. *ACS Omega* **2020**, *5*, 14767–14775. [CrossRef] [PubMed]
25. Xu, X.; Zhang, R.; Xia, W.; Ma, P.; Ma, C.; Pan, Y.; Jiang, J. Density functional theory study of CL-20/nitroimidazoles energetic cocrystals in an external electric field. *Comput. Theor. Chem.* **2022**, *1209*, 113607. [CrossRef]
26. Wu, X.; Li, Y.; Dong, W.-S.; Zhang, J.-G. External electric field-induced phase transition of a series of energetic pentazole crystals: A first-principles study. *Cryst. Growth Des.* **2022**, *22*, 4977–4986. [CrossRef]
27. Wu, X.; Xu, J.; Li, Y.; Zhu, S.; Dong, W.; Zhang, J.-G. Phase transition induced by an external electric field as a buffer to facilitate the initial decomposition of a series of catenated nitrogen energetic systems: A first-principles study. *Phys. Chem. Chem. Phys.* **2022**, *24*, 12488–12500. [CrossRef] [PubMed]
28. Politzer, P.; Murray, J.S.; Lane, P. Computational determination of effects of electric fields upon "trigger linkages" of prototypical energetic molecules. *Int. J. Quantum Chem.* **2009**, *109*, 534–539. [CrossRef]
29. Sultan, M.; Wu, J.; Haq, I.U.; Mudassar, M.; Yang, L.; Wu, J.; Lu, J.; Chen, L. A complete thermal decomposition mechanism study of an energetic-energetic CL-20/DNT cocrystal at different extreme temperatures by using ReaxFF reactive molecular dynamics simulations. *J. Mol. Struct.* **2022**, *1269*, 133691. [CrossRef]
30. Ren, F.-D.; Cao, D.-L.; Shi, W.-J.; You, M.; Li, M. A theoretical prediction of the possible trigger linkage of CH3NO2 and NH2NO2 in an external electric field. *J. Mol. Model.* **2015**, *21*, 145. [CrossRef] [PubMed]

31. Gao, Z.; Gu, Z.; Bo, M.; Zhang, P.; Chu, Y.; Zhu, Y.; Ma, P. External electric field-induced molecular structural evolution and electronic response of BITE-101: A multiscale investigation from molecules to crystals. *New J. Chem.* **2025**, *49*, 13279–13291. [CrossRef]
32. Russell, T.P.; Miller, P.J.; Piermarini, G.J.; Block, S. Pressure temperature phase-diagram of hexanitrohexaazaisowurtzitane. *J. Phys. Chem.* **1993**, *97*, 1993–1997. [CrossRef]
33. Vonholtz, E.; Ornellas, D.; Foltz, M.F.; Clarkson, J.E. The solubility of epsilon-CL-20 in selected materials. *Propellants Explos. Pyrotech.* **1994**, *19*, 206–212. [CrossRef]
34. Foltz, M.F.; Coon, C.L.; Garcia, F.; Nichols, A.L. The thermal stability of the polymorphs of hexanitrohexaazaisowurtzitane, Part II. *Propellants Explos. Pyrotech.* **1994**, *19*, 19–25. [CrossRef]
35. Qiu, L.; Zhu, W.-H.; Xiao, J.-J.; Zhu, W.; Xiao, H.-M.; Huang, H.; Li, J.-S. Molecular dynamics simulations of trans-1,4,5,8-tetranitro-1,4,5,8-tetraazadecalin-based polymer-bonded explosives. *J. Phys. Chem. B* **2007**, *111*, 1559–1566. [CrossRef] [PubMed]
36. Bader, R.F.W. ChemInform Abstract: A Quantum Theory of Molecular Structure and Its Applications. *Chem. Rev.* **1991**, *91*, 893–928. [CrossRef]
37. Espinosa, E.; Molins, E.; Lecomte, C. Hydrogen bond strengths revealed by topological analyses of experimentally observed electron densities. *Chem. Phys. Lett.* **1998**, *285*, 170–173. [CrossRef]
38. Zhang, J.; Guo, W. Roles of Small Molecules in the Stability and Sensitivity of CL-20-Based Host–Guest Explosives under Electric Fields: A Reactive Molecular Dynamics Study. *J. Phys. Chem. A* **2022**, *126*, 286–295. [CrossRef] [PubMed]
39. Chen, R.; Zhang, J.; Chen, H.; Li, G.; Hu, J.; Zhang, H.; Wang, B. Toughening mechanism of phthalonitrile polymer: MD simulation and experiment. *Compos. Sci. Technol.* **2022**, *232*, 109841. [CrossRef]
40. Hehre, W.J.; Ditchfield, R.; Pople, J.A. Self-Consistent Molecular-Orbital Methods. XII. Further Extensions of Gaussian—Type Basis Sets for Use in Molecular-Orbital Studies of Organic Molecules. *J. Chem. Phys.* **1972**, *56*, 2257–2261. [CrossRef]
41. Frisch, M.J.; Trucks, G.W.; Schlegel, H.B.; Scuseria, G.E.; Robb, M.A.; Cheeseman, J.R.; Scalmani, G.; Barone, V.; Mennucci, G.A.; Petersson, G.A.; et al. *Gaussian 09*, Revision E.01; Gaussian, Inc.: Wallingford, CT, USA, 2013.
42. Lu, T.; Chen, F.W. Multiwfn: A Multifunctional Wavefunction Analyzer. *J. Comput. Chem.* **2012**, *33*, 580–592. [CrossRef] [PubMed]
43. Lu, T. A comprehensive electron wavefunction analysis toolbox for chemists, Multiwfn. *J. Chem. Phys.* **2024**, *161*, 082503. [CrossRef] [PubMed]
44. Humphrey, W.; Dalke, A.; Schulten, K. VMD: Visual Molecular Dynamics. *J. Mol. Graph.* **1996**, *14*, 33–38. [CrossRef] [PubMed]
45. Pan, Y.-J.; Jiang, Y.-X. Analyses of the influences of molecular vacancy defect on the geometrical structure, electronic structure, and vibration characteristics of hexogeon energetic material. *Acta Phys. Sin.* **2015**, *64*, 243102. [CrossRef]
46. Chen, F.; Zhou, T.; Li, J.; Wang, X.; Cao, D.; Wang, J.; Yang, Z. Crystal morphology of dihydroxylammonium 5,5′-bistetrazole-1,1′-diolate (TKX-50) under solvents system with different polarity using molecular dynamics. *Comput. Mater. Sci.* **2019**, *168*, 48–57. [CrossRef]

Disclaimer/Publisher's Note: The statements, opinions and data contained in all publications are solely those of the individual author(s) and contributor(s) and not of MDPI and/or the editor(s). MDPI and/or the editor(s) disclaim responsibility for any injury to people or property resulting from any ideas, methods, instructions or products referred to in the content.